Seasonal Eddy Variability in the Northwestern Tropical Atlantic Ocean

MINGHAI HUANG,[a] YANG YANG,[b,c] AND XINFENG LIANG[a]

[a] *School of Marine Science and Policy, University of Delaware, Lewes, Delaware*
[b] *School of Marine Sciences, Nanjing University of Information Science and Technology, Nanjing, China*
[c] *State Key Laboratory of Marine Environmental Science, College of Ocean and Earth Sciences, Xiamen University, Xiamen, China*

(Manuscript received 4 October 2022, in final form 3 January 2023)

ABSTRACT: Eddies in the northwestern tropical Atlantic Ocean play a crucial role in transporting the South Atlantic Upper Ocean Water to the North Atlantic and connect the Atlantic and the Caribbean Sea. Although surface characteristics of those eddies have been well studied, their vertical structures and governing mechanisms are much less known. Here, using a time-dependent energetics framework based on the multiscale window transform, we examine the seasonal variability of the eddy kinetic energy (EKE) in the northwestern tropical Atlantic. Both altimeter-based data and ocean reanalyses show a substantial EKE seasonal cycle in the North Brazil Current Retroflection (NBCR) region that is mostly trapped in the upper 200 m. In the most energetic NBCR region, the EKE reaches its minimum in April–June and maximum in July–September. By analyzing six ocean reanalysis products, we find that barotropic instability is the controlling mechanism for the seasonal eddy variability in the NBCR region. Nonlocal processes, including advection and pressure work, play opposite roles in the EKE seasonal cycle. In the eastern part of the NBCR region, the EKE seasonal evolution is similar to the NBCR region. However, it is the nonlocal processes that control the EKE seasonality. In the western part of the NBCR region, the EKE magnitude is one order of magnitude smaller than in the NBCR region and shows a different seasonal cycle, which peaks in March and reaches its minimum in October–November. Our results highlight the complex mechanisms governing eddy variability in the northwestern tropical Atlantic and provide insights into their potential changes with changing background conditions.

KEYWORDS: Eddies; Instability; Mesoscale processes

1. Introduction

The northwestern tropical Atlantic Ocean (0°–17°N, 60°–30°W) is characterized by the North Brazil Current (NBC), NBC retroflection (NBCR), and North Equatorial Countercurrent (NECC) (e.g., Rosell-Fieschi et al. 2015; Tuchen et al. 2022; Vallès-Casanova et al. 2022). When the NBC meanders and retroflects into the NECC, energetic eddies, namely, NBC rings or eddies, are shed. Previous studies from field observations and numerical simulations show that these eddies account for 20%–50% of the upper-ocean cross-gyre transport of the Atlantic meridional overturning circulation (AMOC; Richardson et al. 1994; Fratantoni et al. 1995; Goni and Johns 2001; Garzoli et al. 2003; Mélice and Arnault 2017). As a critical part of the surface pathway of AMOC, the NBC and associated rings/eddies serve as an interhemispheric conduit for transporting water masses and heat from the South Atlantic to the North Atlantic (Goni and Johns 2003).

Eddies in the northwestern tropical Atlantic Ocean also have far-reaching impacts on the Caribbean Sea and even the Gulf of Mexico. Numerical simulations suggested that some NBC eddies could make their way into the Caribbean Sea and then grow under mixed instabilities (Murphy et al. 1999). Observations of the transport in the southern passages of the Lesser Antilles also displayed substantial variabilities on time scales of 30–80 days, which were attributed to the northwestward propagation of the NBC eddies that interacted with the island arc topography (Wilson and Johns 1997; Johns et al. 2002; van der Boog et al. 2019, 2022). Recent studies show that some of the eddies or variabilities passing over the Lesser Antilles can propagate into the Caribbean Sea, impact the Yucatan Channel transport (van Westen et al. 2018), and even enter the Gulf of Mexico and modify the path of the Loop Current (LC) (e.g., Huang et al. 2021).

Considering the importance of these eddies in transporting ocean properties and materials, and their far-reaching impacts on regional seas, it is necessary to understand their variabilities and the underlying mechanisms. Among many of the temporal scales, here we focus on the seasonal variability, one of the most robustly observed temporal signals. The statistics of the seasonality of the NBC eddies have been examined before based on either altimetry data or numerical models. In earlier studies, no significant seasonality was reported (Goni and Johns 2003). Later, increased eddy generation frequency was reported in the second half of the year by Sharma et al. (2009) but in the first two trimesters by Mélice and Arnault (2017) and Jochumsen et al. (2010). Recently, the highest eddy generation frequency in winter was reported (Aroucha et al. 2020). Apparently, previous conclusions about the seasonal variability of NBC rings are not consistent. Further investigation of the seasonality of eddies in this region is needed.

Most of the previous studies on eddies in the northwestern tropical Atlantic Ocean are based on altimetry data. However, those studies could not inform us about the vertical structure of those eddies (e.g., Wilson et al. 2002). Besides, the altimetry-based analysis may include bias due to the geostrophic approximation, which neglects inertial and other ageostrophic components of the total velocity (Douglass and

---

Corresponding author: Minghai Huang, minghaih@udel.edu

DOI: 10.1175/JPO-D-22-0200.1

Richman 2015; Aroucha et al. 2020). For certain eddies (e.g., Vmax = 1 m s^{-1}, radius = 130 km), the error of geostrophic approximation could increase from 30% at 15°N to 75% at 4°N (Castelão 2011). Using altimetry data only to characterize the eddy features may produce misleading results, especially near the equator. An analysis combining ocean circulation model outputs and satellite observations is beneficial for better understanding the vertical structure and dynamics of eddies in the northwestern tropical Atlantic.

Eddy kinetic energy (EKE) and its temporal variation have been widely examined in global ocean studies (Ferrari and Wunsch 2009; Rieck et al. 2015; Chen et al. 2015; Wang et al. 2019; Yang and Liang 2019a,b; Yang et al. 2020). The seasonal EKE variability can be induced by various dynamical processes, such as barotropic and baroclinic instabilities (e.g., Ferrari and Wunsch 2009). The seasonally varying background flow field and the thermal structure likely modify the barotropic and baroclinic instabilities and hence the seasonal EKE variability. This mechanism has been reported in many parts of the global ocean, such as the East Philippines (Zhang et al. 2021), the Kuroshio Extension (Wang and Pierini 2020; Yang and Liang 2018), the Gulf Stream (Kang et al. 2016; Kang and Curchitser 2017), and the Caribbean Sea (Jouanno et al. 2012). In addition, nonlocal processes, like advection or pressure work, radiated from (or to) the remote region, and dissipation could also influence the EKE variation (Chen et al. 2014; Yang et al. 2017).

In contrast to the regions mentioned above, fewer studies have been conducted to examine the EKE variability in the northwestern tropical Atlantic. In this region, the NBC volume transport can vary from a few Sverdrups (Sv; 1 Sv ≡ 10^6 m^3 s^{-1}) in spring to more than 35 Sv in late summer/early autumn (Johns et al. 1998; Barnier et al. 2001; de Freitas Assad et al. 2020). In addition, the NBC retroflects into the NECC from about July to January with high NBC transport, and then decays or even disappears in spring when the NBC transport is much reduced. Moreover, a recent transport estimate (Tuchen et al. 2020; Fu et al. 2022) in the 10°N NBC region, i.e., the west side of the NBC retroflection, shows large transport during spring but relatively low transport in fall, which is substantially different from the transport seasonality in the NBC reflection region. It is expected that the seasonally varying NBC and other regional transport will modify the mesoscale instabilities.

In addition, Aguedjou et al. (2019) recently examined the EKE and its seasonal variability in the tropical Atlantic Ocean based on altimetry dataset. They found a joint seasonal evolution (i.e., weakest in May and strong in September/October) between the regional EKE and the NBC transport. They also examined the barotropic instability by investigating whether the mean flow met the Rayleigh criterion. Their results suggested that barotropic instability likely occurs in the NECC and east of the NBCR region, while other processes, which were not further analyzed in their study, could be responsible for the eddy generation in the NBCR region. Up to now, as we are aware of, the relative contributions of different processes to the seasonal eddy variability in different regions of the northwestern tropical Atlantic are still unclear.

In this study, six sets of ocean reanalysis data and satellite measurements are used to describe and investigate the seasonal variability of the EKE and the underlying processes in the northwestern tropical Atlantic Ocean, particularly in the most energetic NBCR region and its surrounding areas. The rest of the paper is organized as follows: section 2 briefly introduces the method and section 3 describes the datasets. Section 4 presents the results of the seasonal EKE variability and the governing processes. The results are summarized and discussed in section 5.

2. Methods

We use a recently developed time-varying multiscale energetics framework to investigate the seasonal evolution of EKE in the northwestern tropical Atlantic Ocean. In contrast to other methods, an accurate representation of the multiscale energies and canonical energy transfer can be achieved with this method. A brief description of this method is provided below. For more detailed information about this method, refer to Liang (2016).

This time-varying multiscale energetics framework is based on a new functional analysis apparatus, namely, multiscale window transform (MWT; Liang and Anderson 2007). With MWT, one can split a function space into a set of orthogonal subspaces while retaining its temporal locality. For instance, consider an example flow field, $u = u(t)$, which can be decomposed into a nonstationary mean flow component $u^{\sim 0}(t)$ and eddy flow component $u^{\sim 1}(t)$:

$$u(t) = u^{\sim 0}(t) + u^{\sim 1}(t), \tag{1}$$

where $u^{\sim\varpi}(t)$, like a filtered series, is called the multiscale window reconstruction (MWR) of $u(t)$ on scale window ϖ ($\varpi = 0, 1$). Liang and Anderson (2007) found that, for each $u^{\sim\varpi}(t)$, there exists a corresponding transform coefficient $\widehat{u}_n^{\sim\varpi}$ [$\widehat{(\cdot)}_n^{\sim\varpi}$ denotes MWT on window ϖ at time step n]. The time-dependent multiscale energy on scale window ϖ proves to be proportional to $(\widehat{u}_n^{\sim\varpi})^2$. See the appendix for more details on the multiscale energy presentation.

Within the MWT framework, the kinetic energy (KE) and the available potential energy (APE) on scale window ϖ can be defined as

$$K^\varpi = \frac{1}{2}\widehat{\mathbf{v}}_h^{\sim\varpi} \cdot \widehat{\mathbf{v}}_h^{\sim\varpi}, \tag{2}$$

$$A^\varpi = \frac{1}{2}c\,(\widehat{\rho}^{\sim\varpi})^2, \tag{3}$$

where $\mathbf{v}_h$ is the horizontal velocity, $c = g^2/\rho_0^2N^2$, N is the Brunt–Väisälä frequency, ρ_0 is the reference density (1025 kg m^{-3}), and ρ is the density anomaly [with the mean vertical profile $\underline{\rho}(z)$ removed]. For notational simplicity, the dependence on n is suppressed. The MWT-based multiscale ocean energetic equations for the multiscale KE (K^ϖ) and APE (A^ϖ) can also be obtained as

$$\frac{\partial K^{\varpi}}{\partial t} = \underbrace{-\nabla\cdot\left\{\frac{1}{2}[\widehat{(\mathbf{v}\mathbf{v}_h)}^{\sim\varpi}\cdot\widehat{\mathbf{v}}_h^{\sim\varpi}]\right\}}_{-\nabla\cdot\mathbf{Q}_k^{\varpi}}$$

$$+\underbrace{\frac{1}{2}[\widehat{(\mathbf{v}\mathbf{v}_h)}^{\sim\varpi}:\nabla\widehat{\mathbf{v}}_h^{\sim\varpi}-\nabla\cdot\widehat{(\mathbf{v}\mathbf{v}_h)}^{\sim\varpi}\cdot\mathbf{v}_h^{\sim\varpi}]}_{\Gamma_k^{\varpi}}$$

$$\underbrace{-\nabla\cdot\left(\frac{1}{\rho_0}\widehat{\mathbf{v}}^{\sim\varpi}\widehat{\mathbf{P}}^{\sim\varpi}\right)}_{-\nabla\cdot\mathbf{Q}_P^{\varpi}}+\underbrace{\left(-\frac{g}{\rho_0}\widehat{\rho}^{\sim\varpi}\widehat{\mathbf{w}}^{\sim\varpi}\right)}_{b^{\varpi}}+F_K^{\varpi}, \qquad (4)$$

$$\frac{\partial A^{\varpi}}{\partial t} = \underbrace{-\nabla\cdot\left[\frac{1}{2}c\widehat{\rho}^{\sim\varpi}\widehat{(\mathbf{v}\rho)}^{\sim\varpi}\right]}_{-\nabla\cdot\mathbf{Q}_A^{\varpi}}$$

$$+\underbrace{\frac{c}{2}[\widehat{(\mathbf{v}\rho)}^{\sim\varpi}\cdot\nabla\widehat{\rho}^{\sim\varpi}-\rho^{\sim\varpi}\nabla\cdot\widehat{(\mathbf{v}\rho)}^{\sim\varpi}]}_{\Gamma_A^{\varpi}}$$

$$+\underbrace{\frac{g}{\rho_0}\widehat{\rho}^{\sim\varpi}\widehat{\mathbf{w}}^{\sim\varpi}}_{-b^{\varpi}}+\underbrace{\frac{1}{2}\widehat{\rho}^{\sim\varpi}\widehat{(\mathbf{w}\rho)}^{\sim\varpi}\frac{\partial c}{\partial z}}_{S_A^{\varpi}}+F_A^{\varpi}. \qquad (5)$$

The colon operator ":" is defined such that, for two dyadic products **AB** and **CD**, $(\mathbf{AB}):(\mathbf{CD}) = (\mathbf{A}\cdot\mathbf{C})(\mathbf{B}\cdot\mathbf{D})$. The change rates of KE and APE on the left-hand side are determined by the processes on the right-hand side, where $-\nabla\cdot\mathbf{Q}_k^{\varpi}$ and $-\nabla\cdot\mathbf{Q}_A^{\varpi}$ are the energy flux convergence of K^{ϖ} and A^{ϖ}, respectively, representing the advection of energy. The term $-\nabla\cdot\mathbf{Q}_P^{\varpi}$ is the pressure flux convergence. The terms Γ_k^{ϖ} and Γ_A^{ϖ} are cross-scale transfers of KE and APE to window ϖ from other windows, standing for the redistribution of energy among different scales (Fig. 1). The b^{ϖ} terms are the buoyancy conversion between KE and APE on the designated scale window. The term S_A^{ϖ} is the result from the vertical shear of c (a source/sink of A^{ϖ} and usually negligible). The residual terms F_K^{ϖ} and F_A^{ϖ} include contributions from friction, external forcing, and subgrid processes. The meaning of each term in Eqs. (4) and (5) is summarized and presented in Table 1.

Note that the cross-scale transfer holds the following property,

$$\sum_{\varpi}\sum_{n}\Gamma_n^{\varpi} = 0,$$

indicating that the transfer is merely a redistribution of energy among windows of different scales. This simple property is not met in traditional formalisms (see the appendix for more details). To distinguish this from the traditional way, they are called canonical transfers. Liang and Robinson (2007) demonstrated that canonical transfers correspond precisely to the classical barotropic and baroclinic instabilities. In this study, we use the superscript 0 → 1 to represent the transfer from the mean flow window ($\varpi = 0$) to the eddy window ($\varpi = 1$). The canonical transfer of KE (APE) from the mean flow window to the eddy window is denoted as $\Gamma_k^{0\to1}$ ($\Gamma_A^{0\to1}$). A positive $\Gamma_k^{0\to1}$ ($\Gamma_A^{0\to1}$) represents a release of mean flow KE (APE) to mesoscale eddies, indicating the occurrence of barotropic (baroclinic) instability. For this reason, hereinafter $\Gamma_k^{0\to1}$ and $\Gamma_A^{0\to1}$ are called barotropic transfer (BT) and baroclinic transfer (BC), respectively. These time–space-dependent canonical transfer matrices and other energetics terms appearing on the right-hand sides of Eqs. (4) and (5) allow us to quantify the spatiotemporal variations associated with the seasonal eddy variability.

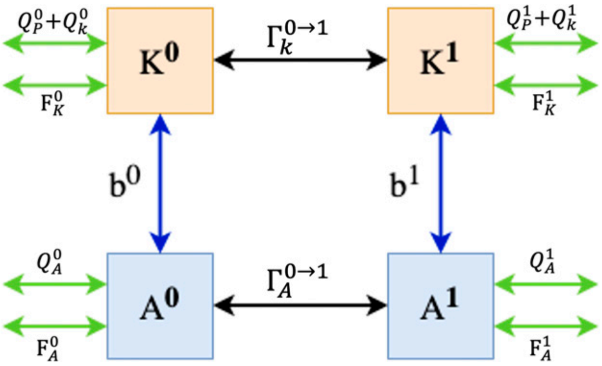

FIG. 1. A schematic of the multiscale energy pathway for a two-window decomposition. The letter K represents KE and A represents APE. Black arrows indicate the energy transfers between the mean–flow window (indicated by superscript 0) and the eddy window (indicated by superscript 1). Blue arrows represent the buoyancy conversion connecting the KE and APE reservoirs. Green arrows indicate nonlocal processes. The forcing and dissipation processes are denoted as F terms (green arrows).

Besides $\Gamma_A^{0\to1}$ (i.e., $A^0 \to A^1$), the buoyancy conversion b^1 in the EKE budget equation (i.e., $A^1 \to K^1$) is also widely used to indicate baroclinic instability. The two processes form the typical energy pathway (i.e., $A^0 \to A^1 \to K^1$) in a baroclinic instability system. It should be noted that buoyancy conversion, though important itself, is a physical concept that does not necessarily reflect baroclinic instability. This has been argued in previous studies such as Liang and Robinson (2009). For example, in the ocean, strain-induced frontogenesis is featured with a significant conversion from eddy APE to EKE due to the setup of a secondary overturning circulation, but it does not indicate the occurrence of baroclinic instability (McWilliams 2016). That said, in section 3, both $\Gamma_A^{0\to1}$ and b^1 are analyzed to study the baroclinic instability of the NBC system.

To separate the background flow and eddies with the MWT approach, we need to choose the eddy scale level, a cutoff time period of eddies. Early studies from mooring observation showed that NBC rings have deep-reaching 40–60- and 60–90-day oscillations and surface-trapped 25–40-day fluctuations (Johns et al. 1990, 1998). In addition, Castelão (2011) analyzed 18 years satellite altimetry observation and found that the time interval between successive rings is 20–170 days. Also based on altimetry dataset, a recent study by Aguedjou et al. (2019) showed that the lifetime of mesoscale eddies in this region is usually shorter than 120 days.

To accurately choose the eddy scale level, we conduct a wavelet analysis (Liu et al. 2007) of the normalized meridional

TABLE 1. Multiscale energetic terms in Eqs. (4) and (5). For details, see Liang (2016).

Symbol	Mathematical form	Meaning
K^{ϖ}	$\frac{1}{2}\widehat{\mathbf{v}}_h^{\sim\varpi}\cdot\widehat{\mathbf{v}}_h^{\sim\varpi}$	KE on scale window ϖ
$\mathbf{Q}_k^{\varpi}$	$\frac{1}{2}[\widehat{(\mathbf{v}\mathbf{v}_h)}^{\sim\varpi}\cdot\widehat{\mathbf{v}}_h^{\sim\varpi}]$	KE flux on window ϖ
Γ_k^{ϖ}	$\frac{1}{2}[\widehat{(\mathbf{v}\mathbf{v}_h)}^{\sim\varpi}:\nabla\widehat{\mathbf{v}}_h^{\sim\varpi}-\nabla\cdot\widehat{(\mathbf{v}\mathbf{v}_h)}^{\sim\varpi}\cdot\mathbf{v}_h^{\sim\varpi}]$	Canonical transfer of KE to window ϖ
$\mathbf{Q}_P^{\varpi}$	$\frac{1}{\rho_0}(\widehat{\mathbf{v}}^{\sim\varpi}\widehat{\mathbf{P}}^{\sim\varpi})$	Pressure flux on window ϖ
b^{ϖ}	$-\frac{g}{\rho_0}\widehat{\rho}^{\sim\varpi}\widehat{\mathbf{w}}^{\sim\varpi}$	Buoyancy conversion on window ϖ
A^{ϖ}	$\frac{1}{2}c(\widehat{\rho}^{\sim\varpi})^2, c=\frac{g^2}{\rho_0^2N^2}$	APE on window ϖ
$\mathbf{Q}_A^{\varpi}$	$\frac{1}{2}[c\widehat{\rho}^{\sim\varpi}\widehat{(\mathbf{v}\rho)}^{\sim\varpi}]$	APE flux on window ϖ
Γ_A^{ϖ}	$\frac{c}{2}[\widehat{(\mathbf{v}\rho)}^{\sim\varpi}\cdot\nabla\widehat{\rho}^{\sim\varpi}-\rho^{\sim\varpi}\nabla\cdot\widehat{(\mathbf{v}\rho)}^{\sim\varpi}]$	Canonical transfer of APE to window ϖ
S_A^{ϖ}	$\frac{1}{2}\widehat{\rho}^{\sim\varpi}\widehat{(\mathbf{w}\rho)}^{\sim\varpi}\frac{\partial c}{\partial z}$	Apparent source/sink of A^{ϖ} (usually negligible)
F_K^{ϖ}, F_A^{ϖ}	Not explicitly expressed but treated as a residue term in the KE/APE budget equation	Dissipation/diffusion of KE/APE on window ϖ through subgrid processes

velocity (the anomaly divided by the standard deviation) calculated from altimetry data at the east side of NBCR (NBCR East: 3.625°N, 40.625°W), NBCR (7.625°N, 51.375°W), and the west side of NBCR (NBCR West: 10.375°N, 56.625°W). Figure 2 shows that in the most energetic NBCR region, besides the annual signal, the energy is mostly confined to the 16–160-day band and has a peak around 48 days, consistent with previous studies (e.g., van Westen et al. 2018). Compared to the most energetic NBCR region, NBCR West is less energetic with a peak around 40 days which has been found related to the propagation of NBC eddies (Johns et al. 2002; Aroucha et al. 2020). In NBCR East, the spectrum shape moves toward the low-frequency side with a peak around 112 days. So, based on previous studies and the wavelet analysis results, a period shorter than 160 days seems to be a reasonable choice for the upper bound of the mesoscale window. We have also tested 128 days and 192 days as the scale level bound, and the results are all quantitatively similar.

It should be noted that intraseasonal variability also appears in the study region, particularly in the NBCR East (Körner et al. 2022). Previous studies reported that low-baroclinic-mode Yanai waves with periods of about 30 days are generated to the east side of 40°W, and high-baroclinic-mode Yanai waves with periods between 30 and 40 days are excited between the NBC and the Equatorial Undercurrent (e.g., Körner et al. 2022). In addition, the typical tropical instability waves (TIWs) with period between 20 and 40 days also appear in the NBCR East but are more pronounced in the central Atlantic (Jochum et al. 2004; von Schuckmann et al. 2008; de Decco et al. 2018). However, these high-frequency variabilities are not the dominant energy components as shown in the power spectrum (Fig. 2a). We therefore do not make a specific distinction between eddy and the high-frequency intraseasonal variability in the NBCR East.

Two samples showing the separation of eddies and background flows are presented in Fig. 3. Clearly, the original sea surface height and velocity fields show the combination of eddies, NBC, and NBC retroflection (Figs. 3a,d). After applying the MWT, one can see that the NBC eddies are well separated from the background field (Figs. 3c,f). The nonstationary background field including the NBC and NBCR are shown in Figs. 3b,e.

3. Data

a. Ocean reanalysis products

To ensure the robustness of our analysis, we utilize six global ocean reanalysis products, i.e., Estimating the Circulation and Climate of the Ocean, Phase 2 (ECCO2), Hybrid Coordinate Ocean Model with Naval Research Laboratory Coupled Ocean Data Assimilation (HYCOM + NCODA, hereinafter HYCOM for brevity), and four additional products released by Copernicus Marine Environment Monitoring Service (CMEMS), namely, Global Ocean Reanalysis and Simulation from Mercator Ocean (GLOR), ORAS5 from the European Centre for Medium-Range Weather Forecasts; Forecast Ocean Assimilation Model from the Met Office (FOAM), and C-GLORSv7 from Centro Euro-Mediterraneo sui Cambiamenti Climatici (CGLO). A brief description of the six products follows. For more information, refer to Table 2 and the references therein.

ECCO2 is an ocean state estimate based on the Massachusetts Institute of Technology General Circulation Model (MITgcm; Marshall et al. 1997). Various ocean observational data are assimilated using the Green's function approach. As a result, the ECCO2 product is constrained by observations yet is still dynamically and kinematically consistent (Wunsch et al. 2009). This feature is of vital importance for our energetic analysis. Estimates from ECCO2 have a 0.25° × 0.25° horizontal resolution, 50 vertical levels with 3-day time intervals. The temporal range of ECCO2 is from 1992 to 2021. The vertical resolution varies from 10 m near the sea surface to

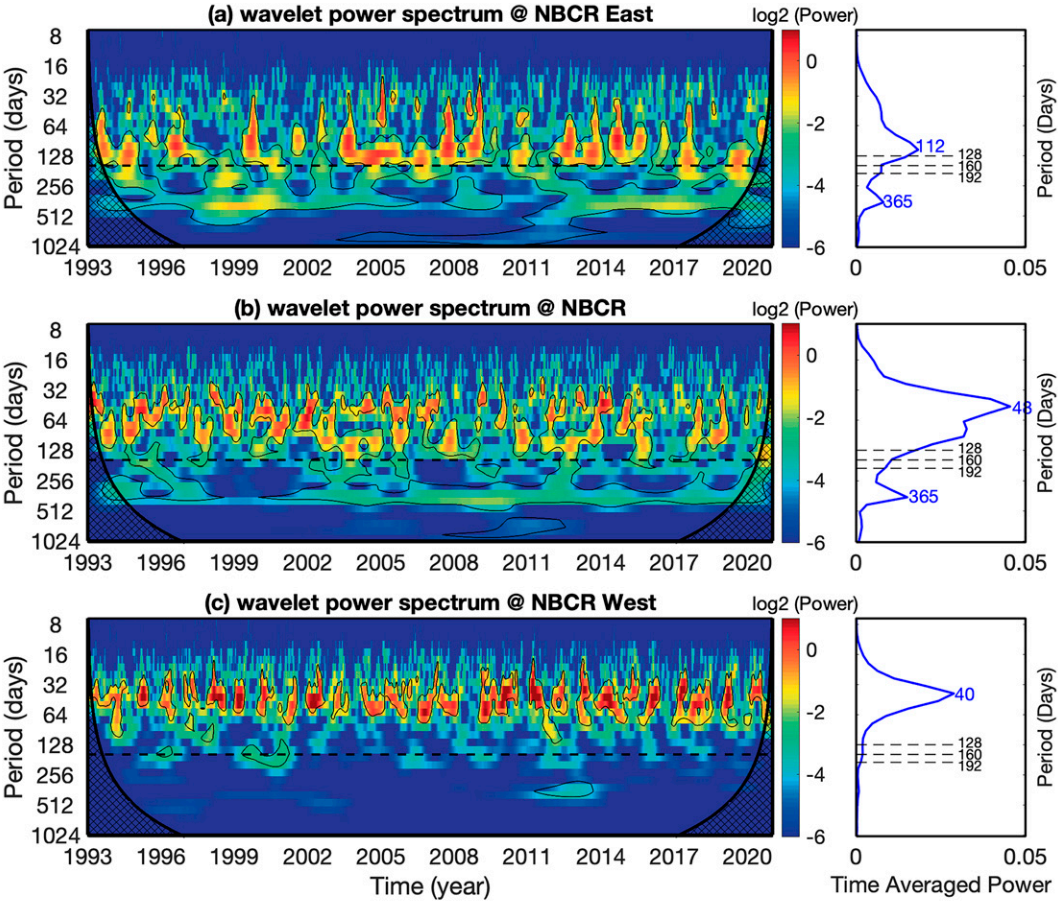

FIG. 2. (left) Rectified wavelet power spectrum in logarithm (base 2) for the normalized meridional velocity at the NBCR East (3.625°N, 40.625°W), NBCR (7.625°N, 51.375°W) and NBCR West (10.375°N, 56.625°W). Black dashed lines mark the cutoff period of 160 days. Cross-hatched regions indicate the “cone of influence,” where edge effects become important. The regions of greater than 95% confidence are shown with black contours. (right) The blue line represents the time-averaged wavelet power spectra and the peak is also marked. Black dashed lines mark the cutoff period of 128, 160, and 192 days. The locations of the three dots are shown in Fig. 3a.

~450 m near the bottom. Refer to Menemenlis et al. (2008) for more information.

The Global Ocean Forecasting System (GOFS) 3.1, which utilizes HYCOM and Navy Coupled Ocean Data Assimilation (NCODA) system, is also used in this study. HYCOM assimilates a large number of observations, from satellite altimetry to in situ oceanic profiles, using the NCODA system (Cummings and Smedstad 2013). The estimates are eddy-resolving with a horizontal resolution of 1/12°, 40 vertical levels with daily time interval. The temporal range of HYCOM is from 1994 to 2016. The vertical resolution varies from 2 m near the sea surface to 1000 m near the bottom. For more information about this product, refer to Metzger et al. (2014).

The other four global ocean reanalyses are from the CMEMS Global Ocean Ensemble Reanalysis project and for simplicity are described together here. All four products are homogeneous 3D gridded descriptions of the physical state of the ocean constrained with satellite and in situ observations (Zuo et al. 2019; Lellouche et al. 2013; Storto and Masina 2016; Blockley et al. 2014). They all have 0.25° × 0.25° horizontal resolution, 75 vertical levels, and daily time intervals. Their temporal range is from 1993 to 2019. The vertical resolution varies from a few meters near the sea surface to ~200 m near the bottom. One can refer to its handbook for more information.

For consistency, all six datasets are interpolated to the same 0.25° × 0.25° horizontal grids with 5-day intervals. Only estimates during their overlapping period 1994 to 2016 are used.

b. *Satellite observation*

We also use the satellite altimetry product from the Copernicus Marine Environment Monitoring Service (CMEMS), which includes the sea level anomalies (SLA), absolute dynamic topography (ADT), and geostrophic currents, to characterize the seasonal surface eddy characteristics. The SLA is referenced to a 20-yr (1993–2012) mean (Pujol et al. 2016). The altimetry data has 0.25° × 0.25° horizontal resolution with daily temporal intervals. For consistency, only the altimetry data from 1994 to 2016 are used in this study.

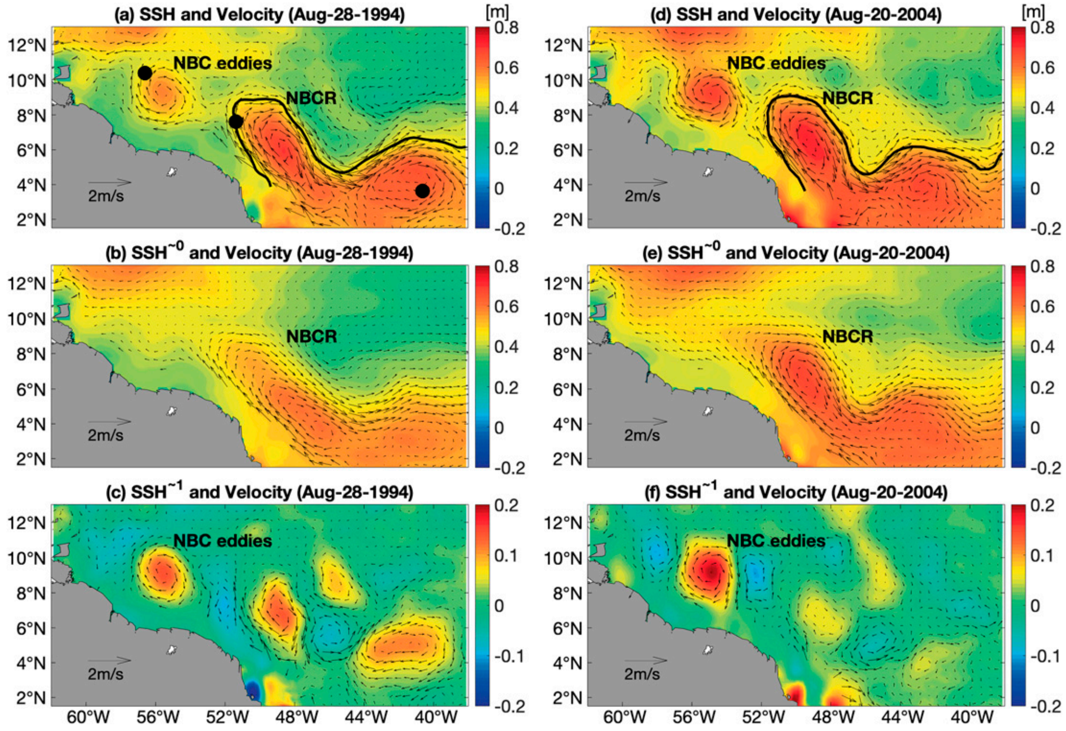

FIG. 3. Altimetry sea surface height (SSH) and geostrophic current on (left) 28 Aug 1994 and (right) 20 Aug 2004: (a),(d) original SSH field; (b),(e) MWT low-pass-filtered components (mean current); (c),(f) MWT high-pass-filtered components (eddies). The black lines in (a) and (d) (the 0.46-, 0.51-m SSH contours) mark the position of the NBC retroflection. The three black dots are used to generate Fig. 2.

4. Results

a. Seasonal variability of EKE

Figures 4a–g show the long-term mean of geostrophic EKE (GeoEKE), which is calculated with sea surface heights from the altimetry data and six ocean reanalysis products by applying the geostrophic approximation. High EKE appears in the northwestern tropical Atlantic Ocean, with the NBCR being the most energetic region. The strength of EKE in each product differs. The GeoEKE in ORAS5, GLOR, and CGLO is smaller than in the altimetry. Other ocean reanalyses (i.e., ECCO2, HYCOM, FOAM) agree well with the altimetry data except the HYCOM data, which show much higher values near the equator than the others. Note that the EKE displayed in Figs. 4a–g is based on geostrophic velocity derived from sea surface height and includes errors associated with the negligence of inertial and other ageostrophic components (Douglass and Richman 2015; Aroucha et al. 2020). As mentioned in the introduction, errors of geostrophic approximation could be large close to the equator.

The surface EKE (Figs. 4h–m), which is calculated with the top-layer total velocity from ocean reanalysis products, is also displayed and compared. The top layers of the six products are 5 m for ECCO, 0 m for HYCOM, and 0.5 m for ORAS5, GLOR, CGLO, and FOAM. As expected, the unrealistic high values appearing south of 3°N in the GeoEKE maps disappear in the surface EKE. The surface EKE generally shows similar spatial patterns to the GeoEKE, but their magnitude is much larger. In addition, we calculate and compare the depth-averaged EKE (Mean EKE) in the upper 200 m, in which the highest EKE is confined (shown later). We also test 600 m as the bottom level of the vertical integration/

TABLE 2. Information of the six ocean reanalysis products and the satellite observations used in this study.

Dataset	Time range	Spatial resolution	Vertical levels	Temporal resolution	Reference
ECCO2	1992–2021	0.25° × 0.25°	50, 5–5906 m	3 days	Menemenlis et al. (2008)
HYCOM	1994–2016	1/12° × 1/12°	40, 0–5000 m	Daily	Metzger et al. (2014)
ORAS5	1993–2019	0.25° × 0.25°	75, 0.5–5902 m	Daily	Zuo et al. (2019)
GLOR	1993–2019	0.25° × 0.25°	75, 0.5–5902 m	Daily	Lellouche et al. (2013)
CGLO	1993–2019	0.25° × 0.25°	75, 0.5–5902 m	Daily	Storto and Masina (2016)
FOAM	1993–2019	0.25° × 0.25°	75, 0.5–5902 m	Daily	Blockley et al. (2014)
Altimetry	1993–2021	0.25° × 0.25°	Surface	Daily	Pujol et al. (2016)

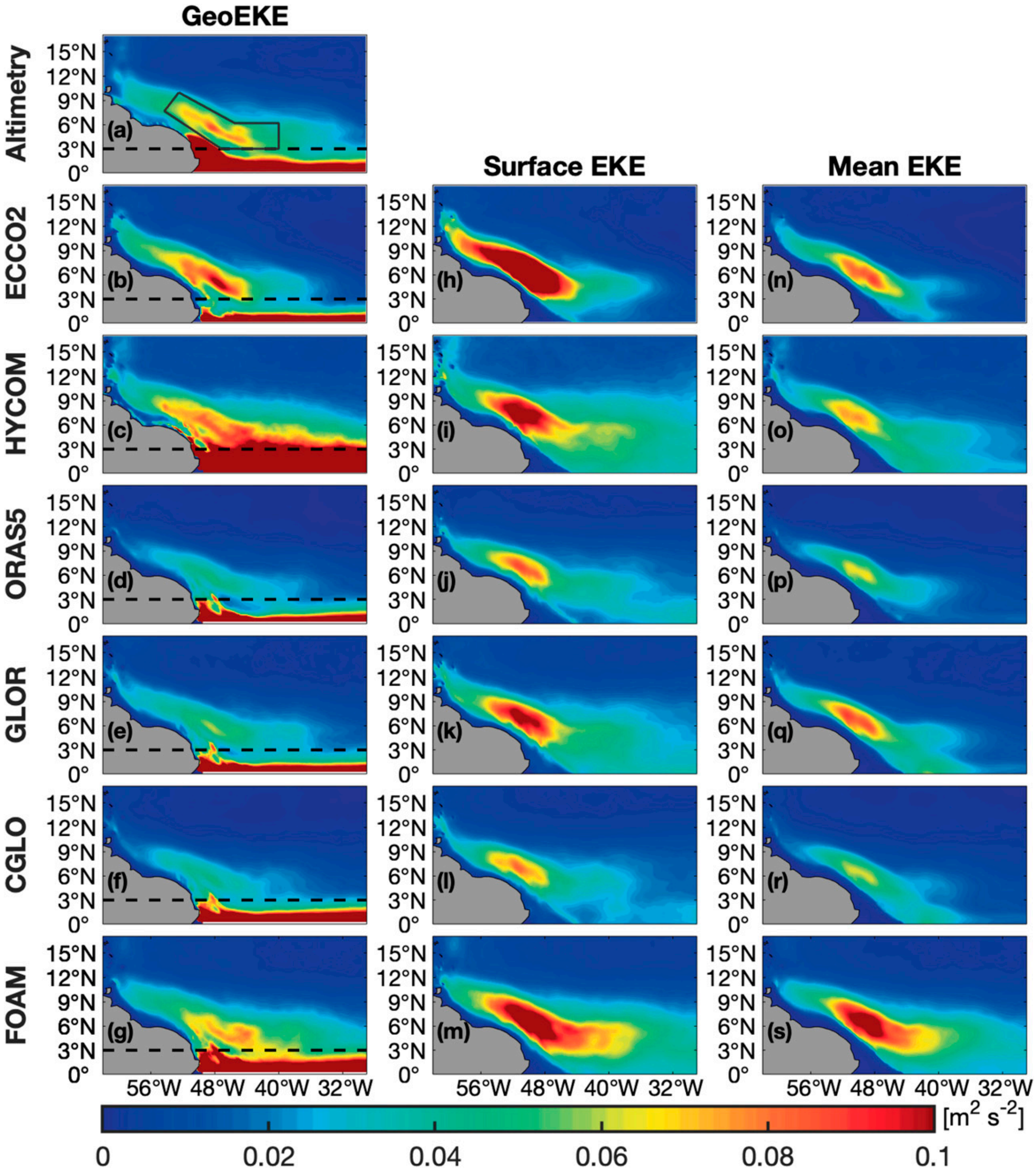

FIG. 4. Geostrophic EKE (m^2 s^{-2}) calculated with sea surface heights from (a) altimetry, (b) ECCO2, (c) HYCOM, (d) ORAS5, (e) GLOR, (f) CGLO, and (g) FOAM. (h)–(m) As in (b)–(g), but for surface (first layer) EKE (m^2 s^{-2}) calculated with the top-layer velocity. (n)–(s) As in (b)–(g), but for depth-mean (upper 200-m depth) EKE. The dashed line in (a)–(g) marks 3°N.

averaging. All the conclusions remain the same. The results (Figs. 4n–s) display similar spatial patterns to the surface EKE, with the NBCR being the most energetic region. Based on their agreement with the altimetry data, particularly in the most energetic NBCR region, and the consistency among them, we consider the selected ocean reanalysis products can be used to evaluate the seasonal EKE variability and the underlying mechanisms in the northwestern tropical Atlantic Ocean.

We then examine the seasonal variation of the EKE averaged over the box marked in Fig. 4a with the six ocean

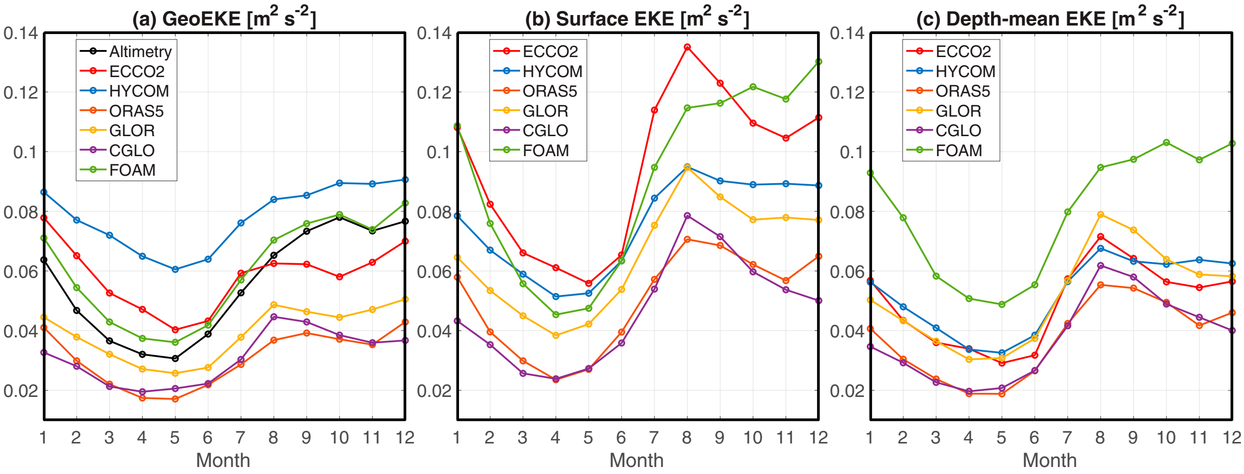

FIG. 5. Seasonal cycle of the area-mean EKE (m^2 s^{-2}) from (a) altimetry and six ocean reanalysis products. (b) EKE of the top layer of the six ocean reanalysis products. (c) As in (b), but for the depth-mean EKE (upper 200 m).

reanalysis products. The seasonal variation of the GeoEKE from all the products is generally consistent in their timing despite the apparent difference in the magnitude. Considering the potential importance of the ageostrophic component (Douglass and Richman 2015; Aroucha et al. 2020), we also examine the total EKE (i.e., surface EKE and depth-mean EKE), which are calculated with velocities from the reanalysis products. Similar to the GeoEKE, the seasonal variation of the surface EKE from the ocean reanalyses except FOAM shows consistent patterns in timing but apparent difference in the magnitude (Fig. 5b). More specifically, all the products except FOAM exhibit an EKE minimum in April–May and an EKE maximum in August. This pattern is even clearer in the depth-mean EKE (upper 200 m) as shown in Fig. 5c.

We further study the spatial pattern of the seasonal EKE variability from the six ocean reanalysis products. As shown in Fig. 6, EKE in the most energetic NBCR region reaches its maximum during July–September (JAS) and minimum during April–June (AMJ) except FOAM. The EKE in JAS is about twice as strong as in AMJ. This result is consistent with the seasonal EKE time series shown in Fig. 5c. It should be noted that during AMJ season, the EKE in the NBCR region reaches its minimum but shows relatively higher EKE in the NBCR West, more specifically from the east side of the Lesser Antilles to the NBCR.

We then further divide the energetic northwestern tropical Atlantic Ocean into three subregions (marked as boxes in Fig. 6c): NBCR East in box 1, NBCR in box 2, and NBCR West in box 3. The seasonal EKE evolutions in the most energetic NBCR and NBCR East regions are basically in phase with each other. In the NBCR West, however, higher EKE in AMJ corresponds to lower NBCR EKE, and the lowest EKE in JAS corresponds to the highest NBCR EKE. Note that the above phenomenon is presented in all the six ocean reanalysis

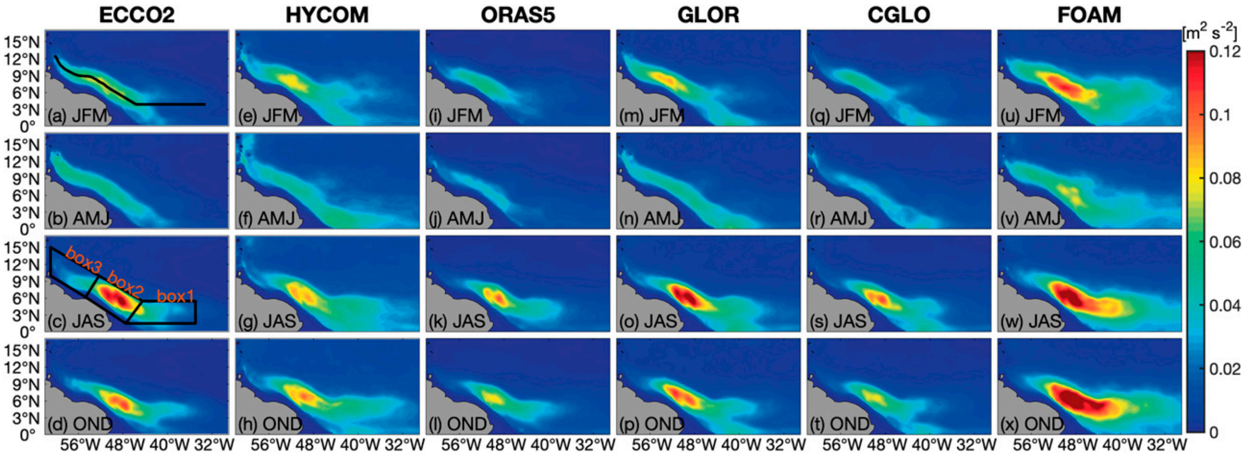

FIG. 6. Seasonal maps of the depth-mean (upper 200-m depth) EKE (m^2 s^{-2}). (a)–(d) ECCO2, (e)–(h) HYCOM, (i)–(l) ORAS5, (m)–(p) GLOR, (q)–(t) CGLO, and (u)–(x) FOAM. Box 2 marks the most energetic NBCR region. Box 1 and box 3 represent the NBCR East and West, respectively. The black line in (a) is used to generate Fig. 8.

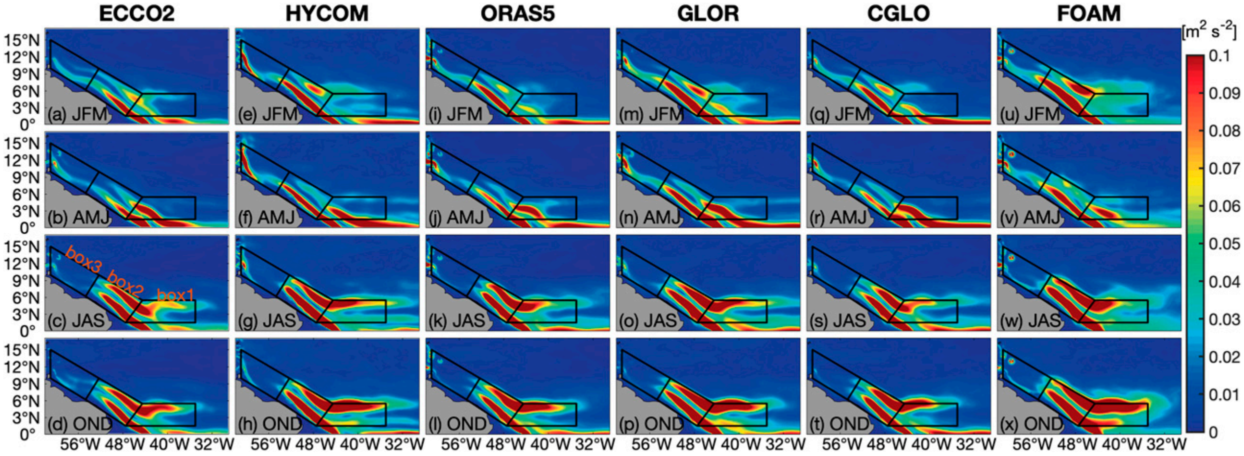

FIG. 7. Seasonal maps of the depth-mean (upper 200 m) MKE (m^2 s^{-2}). (a)–(d) ECCO2, (e)–(h) HYCOM, (i)–(l) ORAS5, (m)–(p) GLOR, (q)–(t) CGLO, and (u)–(x) FOAM. Box 2 marks the most energetic NBCR region. Box 1 and box 3 represent the NBCR East and West, respectively.

products, confirming the robustness of the spatial patterns of seasonal EKE variability in this region.

The seasonal EKE variation described above is highly related to the seasonal mean kinetic energy (MKE, K^0) variability (Fig. 7). In the NBCR region (box 2 in Fig. 6c), strong EKE in JAS and OND correspond to high MKE during retroflection season (Johns et al. 1998; Rosell-Fieschi et al. 2015). This close relationship suggests that the strong horizontal shear of the large-scale circulation can modulate the EKE in this region. In AMJ, both the NBC transport and retroflection decay sharply. This is also synchronized with the low EKE state. In the NBCR West (box 3), the elevated EKE in AMJ is also in phase with the high MKE, that is related to the weak retroflection and the NBC continually moving westward. The opposite happens in JAS and OND. The above-described relationships are shown in all the ocean reanalysis products, confirming their robustness.

To explore the vertical structure of the seasonal EKE variability, we extract the EKE along a section (meridional averaged within ±2° perpendicular to the line) marked in Fig. 6a and display the results in Fig. 8. All the ocean reanalysis

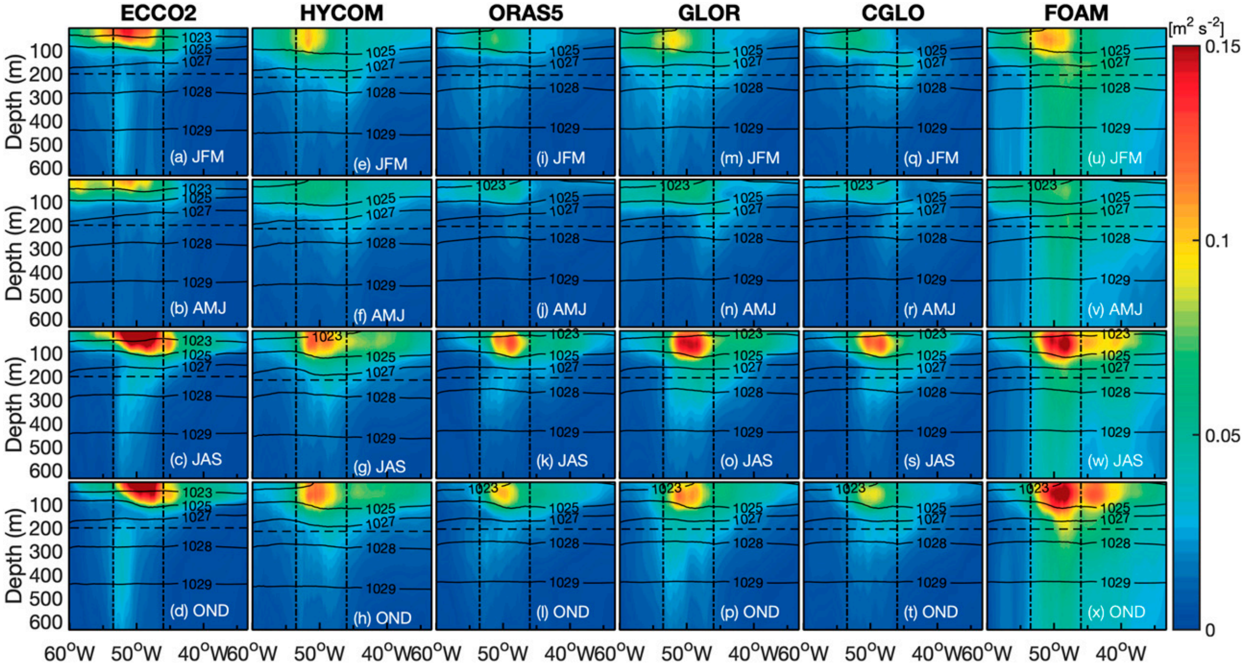

FIG. 8. Vertical structure of EKE (m^2 s^{-2}) and density (black contour; kg m^{-3}) following the line in Fig. 6a. (a)–(d) ECCO2, (e)–(h) HYCOM, (i)–(l) ORAS5, (m)–(p) GLOR, (q)–(t) CGLO, and (u)–(x) FOAM. Black dashed lines mark 200-m depth. The NBCR and the NBCR East and West are separated by two vertical lines.

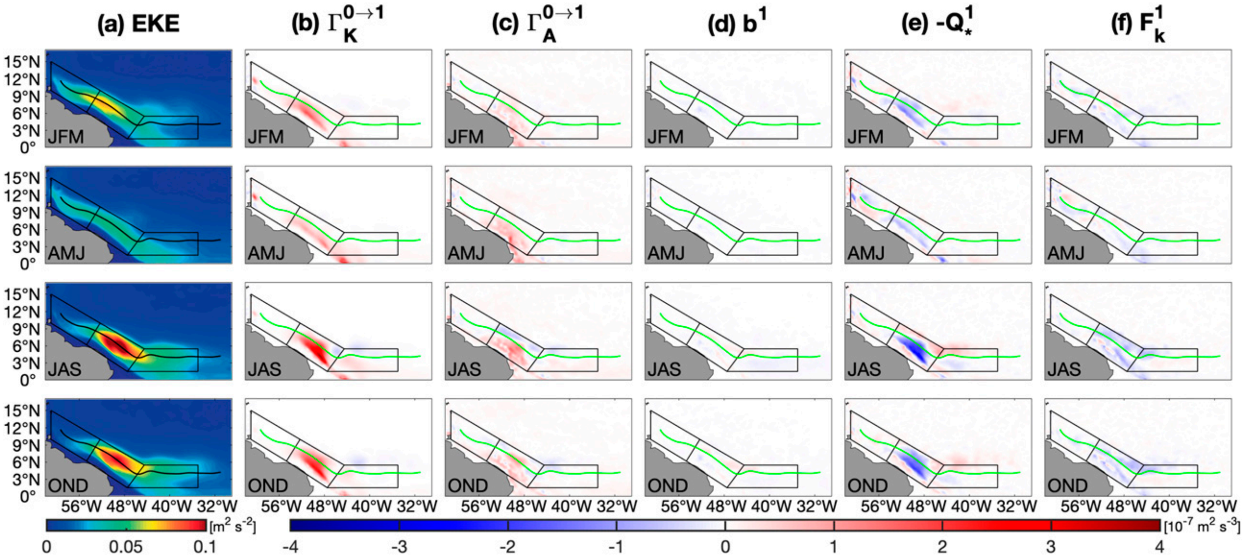

FIG. 9. Seasonal maps of the depth-mean (upper 200 m) EKE and EKE budget terms (m^2 s^{-3}). (a) EKE, (b) barotropic transfer from mean flow to mesoscale eddy window ($\Gamma_k^{0\to1}$), (c) baroclinic transfer from A^0 to A^1 ($\Gamma_A^{0\to1}$), (d) buoyancy conversion rate (b^1), (e) nonlocal processes ($-Q_*^1$), and (f) dissipation F_K^1. The three boxes in Fig. 6a are shown. The black lines in (a) and green lines in (b)–(e) represent the mean eddy trajectory of all the products.

products show that the most energetic signals are confined within the top 200 m. Among the reanalysis products, ECCO2 shows the largest values at sea surface, while the most intensified EKE from HYCOM, ORAS5, GLOR, CGLO, and FOAM appears in the subsurface (~50 m). This explains why the surface EKE in ECCO2 is larger than other products (Fig. 5b) but the depth-mean EKE is of the same magnitude (Fig. 5c). Also, our finding that the largest EKE in this region is confined within the upper 200 m is consistent with previous observational and modeling studies (e.g., Wilson et al. 2002; Jochumsen et al. 2010).

In summary, substantial EKE seasonality is found in the most energetic NBCR region and its east and west sides, and most of the observed seasonality is confined to the top 200 m. In the next subsection, we will use the ocean reanalysis products and the time-varying multiscale energetics framework to explore the underlying dynamics governing the EKE seasonality presented above.

b. Underlying mechanism

Considering the consistency of all the ocean reanalysis products, we use their ensemble mean except FOAM to investigate the processes controlling the seasonal EKE variability in the northwestern tropical Atlantic Ocean. The processes controlling the EKE variations and the corresponding terms in Eqs. (4) and (5) were described in the methods section and are listed in Table 1. In the multiscale energy formalism, $\Gamma_k^{0\to1}$ and $\Gamma_A^{0\to1}$ are transfers of KE and APE, respectively, to the eddy window from the large-scale or mean flow window, standing for the redistribution of energy between eddies and mean flows. The b^1 terms are the buoyancy conversion between KE and APE on the eddy window. The $-\nabla\cdot\mathbf{Q}_k^1$ and $-\nabla\cdot\mathbf{Q}_P^1$ terms are associated with nonlocal processes and their combined effect is denoted as $-Q_*^1$. Positive (negative) $-Q_*^1$ represents the energy transport into (out of) the examined domain. F_K^1 represents the residual term. Note that the residual term F_K^1 includes contributions of internal dissipation and external forcing, both of which are not separately diagnosed because some required variables to achieve that are not available.

Figure 9 shows terms controlling the seasonal EKE variability in the studied region. The lines in Fig. 9 stand for the mean eddy trajectory, which is derived using a velocity geometry-based eddy detection scheme (Nencioli et al. 2010) and the first layer velocity. We first examine the most energetic NBCR region. The elevated barotropic energy transfer ($\Gamma_k^{0\to1}$, Fig. 9b) exhibits the same seasonal evolution pattern as the EKE (Fig. 9a), with the maximum in JAS and the minimum in AMJ. This is consistent with the finding of von Schuckmann et al. (2008), which showed strong BT occurring in the second half of the year in this region. Also, the maximum $\Gamma_k^{0\to1}$ is on the left side of the trajectory. This indicates that in this region because the presence of the NBC, which is associated with strong horizontal shear and usually appears on the left side of the eddy trajectory, mesoscale eddies could gain energy from the mean flow field through barotropic instability.

As indicated in Eqs. (4) and (5) and Fig. 1, $\Gamma_A^{0\to1}$ represents the cross-scale energy transfer between the MAPE and EAPE and can be used as an indicator of baroclinic instability. The term b^1, on the other hand, represents the energy conversion between EAPE and EKE. And b^1 is an inseparable part of baroclinic production of EKE through the $A^0\to A^1\to K^1$ (i.e., MAPE → EAPE → EKE) pathway, which has been used for baroclinic instability identification in many applications as

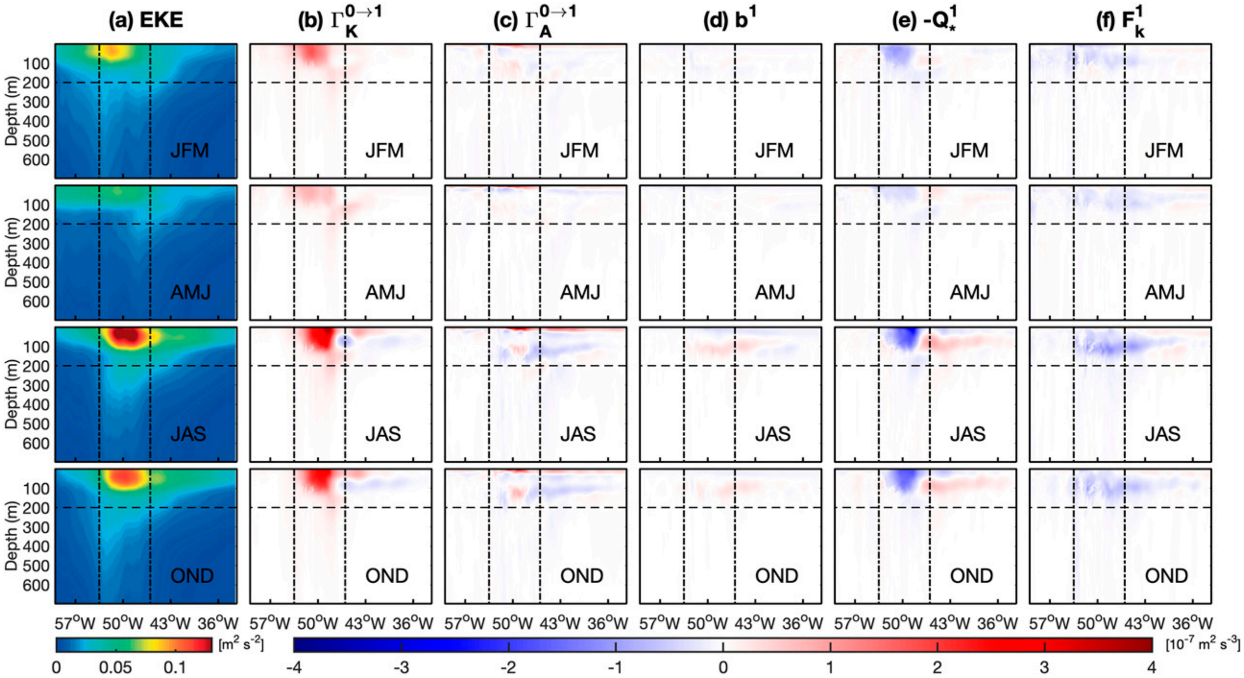

FIG. 10. Vertical structure of the EKE and EKE budget terms (m^2 s^{-3}) following the line marked in Fig. 6a. (a) EKE, (b) barotropic transfer from mean flow to the mesoscale eddy window ($\Gamma_k^{0\to1}$), (c) baroclinic transfer from A^0 to A^1 ($\Gamma_A^{0\to1}$), (d) buoyancy conversion rate (b^1), (e) nonlocal processes ($-Q_*^1$), and (f) dissipation F_K^1. The NBCR and the NBCR East and West are separated by two vertical lines.

well. As shown in Fig. 9c, though there is the transfer from MAPE to EAPE as exhibited in positive $\Gamma_A^{0\to1}$ (da Silveira et al. 2000), it is much smaller than BT ($\Gamma_k^{0\to1}$), and the buoyancy conversion (b^1) is also even smaller than BC. Both terms indicate that baroclinic production of EKE is not likely the process that determines the seasonal EKE modulation. In contrast, the nonlocal term ($-Q_*^1$, Fig. 9e) weighs significantly in the eddy energy budget, indicating that nonlocal processes related to advection and pressure work also play an important role in the local eddy energy budget. The F_K^1 term is small and negative, indicating that dissipation balances the excessive EKE generated by BT and nonlocal process.

In the NBCR East, the nonlocal processes ($-Q_*^1$, Fig. 9e) are more related to the EKE evolution while barotropic energy transfer ($\Gamma_k^{0\to1}$, Fig. 9b) shows positive–negative patches. The baroclinic transfer ($\Gamma_A^{0\to1}$) and buoyancy conversion term (b^1) are still less significant. In this region, it is the nonlocal processes ($-Q_*^1$) rather than the barotropic energy transfer ($\Gamma_k^{0\to1}$) that control the seasonal EKE evolution. In the NBCR West, the magnitudes of all the terms decrease significantly. The barotropic energy transfer ($\Gamma_k^{0\to1}$) shows relatively high values in JFM and AMJ when EKE is also higher. The baroclinic transfer ($\Gamma_A^{0\to1}$) and buoyancy conversion (b^1) are again not significant. In addition, the nonlocal processes ($-Q_*^1$) do not show clear seasonality. Visually, among all the processes, the barotropic energy transfer ($\Gamma_k^{0\to1}$) seems more closely related to the EKE evolution. Note that since the magnitudes of all terms in the NBCR East and West are small, it is challenging to make solid conclusions about their contributions to the seasonal EKE variability. This will thus be further examined in the area-averaged results presented later in this study.

We also examine the vertical structure of each EKE budget term along the line marked in Fig. 6a. The barotropic energy transfer ($\Gamma_k^{0\to1}$, Fig. 10b) exhibits seasonal evolution patterns that are similar to the EKE (Fig. 10a). Also, the maximum barotropic energy transfer appearing in the upper 200 m is consistent with the EKE patterns, further confirming that the barotropic energy transfer controls the seasonal EKE variability in the most energetic NBCR region. The nonlocal process ($-Q_*^1$, Fig. 10d) is negatively correlated to the barotropic energy transfer. The baroclinic transfer ($\Gamma_A^{0\to1}$) and buoyancy conversion (b^1, Fig. 10c) display some positive values around 130 m but are much smaller than the barotropic energy transfer ($\Gamma_k^{0\to1}$) and nonlocal term ($-Q_*^1$), indicating that baroclinic instability plays an insignificant role in the local EKE budget. These results again confirm that barotropic energy transfer and nonlocal processes are the dominant terms in the seasonal EKE variability in the most energetic NBCR region. In the NBCR East, EKE evolution is more related to the nonlocal process. In the NBCR West, the magnitude of budget terms is relatively small and hard to distinguish visually. The quantitative contribution of each term is examined below.

To further quantify the contributions of the various physical processes to the seasonal EKE variability, time series of the depth-mean (upper 200 m) and area-averaged terms presented above over the most energetic NBCR and its east and west sides are calculated and examined (Fig. 11). In the most

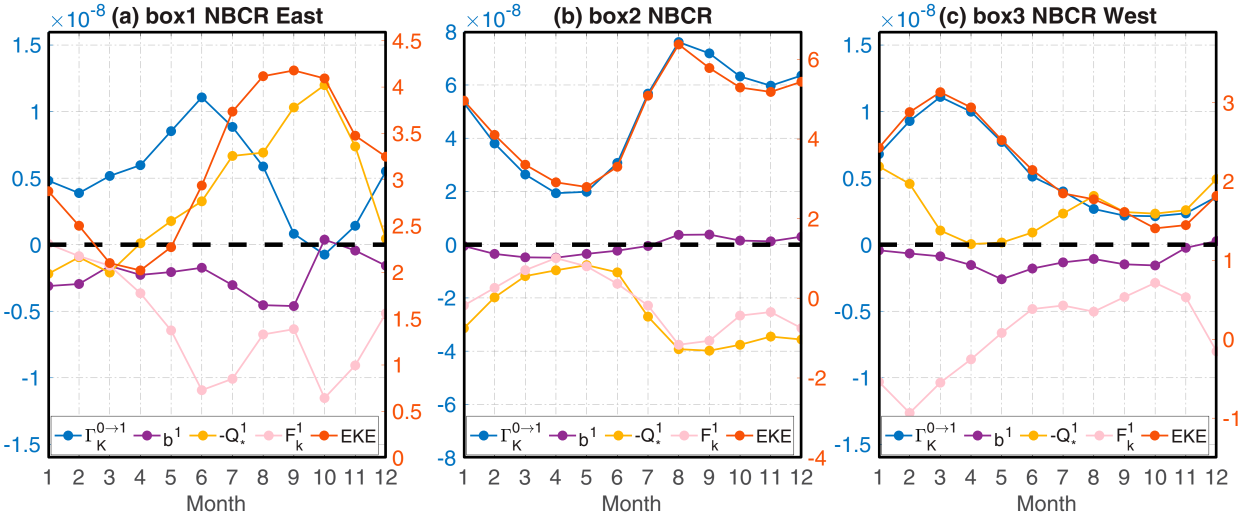

FIG. 11. Seasonal cycle of the area-mean EKE budget terms over the (a) NBCR East (box 1), (b) NBCR (box 2), and (c) NBCR West (box 3). The terms are BT (blue), buoyancy conversion (purple), nonlocal process (yellow), and dissipation (pink). The units of the EKE budget terms and EKE are $\mathrm{m^2\,s^{-3}}$ and $10^{-2}\,\mathrm{m^2\,s^{-2}}$, respectively. The zero solid black lines are used to better distinguish between positive and negative contributions of budget terms. The right *y* axis (red) represents EKE, and the left *y* axis (blue) represents budget terms.

energetic NBCR region (Fig. 11b), the barotropic energy transfer term ($\Gamma_k^{0\to1}$) controls the seasonal EKE variability while the nonlocal process ($-Q_*^1$, KE and pressure flux) and dissipation (F_K^1) play a compensating role. In the NBCR East region (Fig. 11a), the EKE shows similar seasonal variability with a much smaller amplitude than the NBCR region, and it is the nonlocal process and the barotropic energy that control the EKE seasonal variabilities. In particular, the barotropic energy plays a prominent role in the EKE seasonal evolution during the first half of the year. In the NBCR West (Fig. 11c), the seasonal EKE variability is quite different from the NBCR and the NBCR East and the peak EKE appears in spring rather than fall. It could be related to the fact that the NBC could extend northwestward to the NBCR West and reach its maximum speed in spring (Febres-Ortega and Herrera 1976; Richardson and Walsh 1986). Note that the barotropic energy transfer in this region increases and exhibits higher value during spring, consistent with the seasonal movement of NBC.

5. Conclusions and discussion

In this study, we applied a novel time-dependent energetics framework to satellite altimetry data and six ocean reanalysis products to investigate the seasonal variability of EKE in the northwestern tropical Atlantic Ocean and the underlying mechanism. We find that the EKE seasonality and the underlying governing processes are mostly trapped in the upper 200 m and display clear region-dependent patterns. We specifically found the following:

- In the most energetic NBCR region, the EKE peaks in JAS and reaches its minimum in AMJ. The barotropic energy transfer shows the same evolution pattern as EKE and is likely the dominant factor controlling the seasonal EKE evolution in this region.
- In the NBCR East, the EKE seasonal evolution is similar to the NBCR region, peaking in August–October and then reaching its minimum during March–May. However, in this region, it is the nonlocal processes, including advection and pressure work, that play a more important role in the EKE seasonality.
- In the NBCR West, the EKE seasonal cycle is different from both the NBCR and the NBCR East regions. The EKE in this region peaks in March and then gradually decays to its minimum in OND. Similar to the NBCR region, barotropic instability is responsible for the local seasonal EKE variation.

As summarized above, barotropic instability is important for the seasonal EKE variability in most regions of the northwestern tropical Atlantic Ocean. And barotropic instability in this region is related to the NBC, the regionally dominant current. A large number of studies indicate that the NBC can vary on various time scales. For instance, early numerical and observational studies revealed a close link between the intensity of the NBC and the Atlantic meridional overturning circulation (AMOC) on interannual to decadal/multidecadal time scales (Hüttl and Böning 2006; Chang et al. 2008; Zhang et al. 2011; Rühs et al. 2015). Previous studies also found that the Agulhas Leakage (Rühs et al. 2013) and wind-driven variability (Hüttl and Böning 2006) could have a remote impact on the strength of the NBC. Furthermore, recent studies even show the potential effect of climate fingerprint such as the Atlantic Niño (Tuchen et al. 2020; Vallès-Casanova et al. 2022) on the interannual to decadal transport variabilities in the NBC region. Through barotropic instability, a time-varying NBC is likely to alter the EKE in the northwestern tropical Atlantic on longer time scales. Consequently, the seasonality of the eddies in the northwestern tropical Atlantic could show long-term modulations related to climate variabilities and changes. Since some of those eddies could propagate long distance (e.g., Huang et al. 2021), they can potentially act as a route to transfer the large-scale climate signals to regional seas (e.g., Caribbean Sea and Gulf of Mexico). This possibility will be examined in future studies.

In this study, we discussed several but not all dynamical processes that can affect the seasonal EKE variabilities. In particular, previous studies in other regions have shown that submesoscale flows could be important in modulating mesoscale eddies (e.g., Sasaki et al. 2014, 2017; Qiu et al. 2014; Yang et al. 2020). Currently, the submesoscale features cannot be resolved with the ocean reanalysis products used in this study, so their contributions cannot be directly examined. In the future, outputs from super-high-resolution numerical simulations, such as the recent available 1/48° MITgcm simulation (Menemenlis et al. 2008) could be used to further this study, which could bring new insights into the eddy-shedding processes in the NBCR region and its seasonality.

The methodology utilized in this study is a novel time-dependent energetics framework, on the basis of the multiscale window transform (MWT) and the MWT-based canonical energy transfer theory. The MWT based time-varying multiscale energetics framework has been applied with success to a variety of ocean and atmosphere problems such as Kuroshio Extension dynamics, Loop Current eddy shedding in the Gulf of Mexico, eddy shedding into the South China Sea through Luzon Strait, sudden stratospheric warming, atmospheric blocking over the Atlantic Ocean (e.g., Yang and Liang 2018; Yang et al. 2020; Zhao et al. 2016; Xu and Liang 2017; Ma and Liang 2017; Zhao et al. 2022) and could also be applied to other multiscale ocean and atmosphere processes in the future. In addition, the energetics analysis presented in this study is based on a two-scale window decomposition for EKE modulation. It is straightforward to extend the formalism to three or more scale windows and the resulting energy equations are the same in form. Multiscale processes are ubiquitous in ocean and atmosphere, and we can expect more usage of this method in future studies.

Acknowledgments. We thank two anonymous reviewers who provided constructive comments and suggestions and helped us greatly improve this paper. The work was supported in part by National Science Foundation through Grant OCE-2122507.

Data availability statement. ECCO2 and HYCOM can be found from the Asia-Pacific Data-Research Center (http://apdrc.soest.hawaii.edu/data/data.php?discipline_index=2). The satellite altimetry (https://resources.marine.copernicus.eu/productdetail/SEALEVEL_GLO_PHY_L4_MY_008_047/INFORMATION) and ORAS5, GLOR, CGLO, FOAM (https://resources.marine.copernicus.eu/product-detail/GLOBAL_REANALYSIS_PHY_001_031/INFORMATION) model dataset is from the Copernicus Marine Environment Monitoring Service (CMEMS, https://marine.copernicus.eu/).

APPENDIX

Multiscale Window Transform and Canonical Transfer

This appendix provides the necessary information about the multiscale window transform (MWT) and canonical transfer. Most materials in this appendix are similar to the one in a previously published paper (see the appendix in Yang and Liang 2019a). For detailed derivations of the methodology and theory, the reader is referred to Liang (2016).

The multiscale energetics analysis used in this study distinguishes itself from the classical Lorenz formalism (e.g., Lorenz 1955; von Storch et al. 2012) in two aspects. First, the classical Lorenz formalism is formulated with temporal (or zonal) averaging and hence only yields time-mean (or zonal mean) energetics, which is not suitable to evaluate the temporal variability of EKE. To remedy the difficulty, a common practice in literature is to use filters. However, a fundamental but somehow overlooked question is, what is the energy corresponding to a filtered field? To illustrate, consider a field $u(t)$ with only two frequencies ω_0 and ω_1 ($\omega_0 < \omega_1$), which may be filtered into a background part $u^{\sim 0}(t)$ and an eddy part $u^{\sim 1}(t)$, where both parts are functions of t:

$$u(t) = \underbrace{(a_0 \cos\omega_0 t + b_0 \sin\omega_0 t)}_{u^{\sim 0}(t)} + \underbrace{(a_1 \cos\omega_1 t + b_1 \sin\omega_1 t)}_{u^{\sim 1}(t)}. \tag{A1}$$

For the above simple example, the energies for the two parts are the square of their respective Fourier coefficients, i.e., $(a_0^2 + b_0^2)/2$ and $(a_1^2 + b_1^2)/2$, which are absolutely not equal to the square of the corresponding reconstructed (filtered) fields, i.e., $[u^{\sim 0}(t)]^2/2$ and $[u^{\sim 1}(t)]^2/2$. That is to say, multiscale energy is a concept with the transform coefficients defined in phase (frequency) space (independent of t here), while $[u^{\sim 0}(t)]^2/2$ and $[u^{\sim 1}(t)]^2/2$ are quantities in physical space (functions of t). During the past decade, it has been a common practice to use $[u^{\sim 1}(t)]^2/2$ as the time-dependent energy for the eddy part, which is problematic.

It is by no means as trivial a problem to obtain a physically consistent expression of time-dependent multiscale energy. General filters, such as the widely used Butterworth filter, are not suitable here because they only yield reconstructions (i.e., filtered variables), with no transform coefficients. Liang and Anderson (2007) developed MWT for this very purpose. They found that, for a class of specially devised orthogonal filters, there exists a transform–reconstruction pair, which is the MWT and its counterpart, multiscale window reconstruction (MWR). In other words, for each MWR $u^{\sim\varpi}(t)$ (ϖ denotes a specific scale window), there is a corresponding transform coefficient $\widehat{u}_n^{\sim\varpi}$ [$\widehat{(\cdot)}_n^{\sim\varpi}$ denotes MWT on window ϖ at time step n]. The multiscale energy on window ϖ is proved to be $(\widehat{u}_n^{\sim\varpi})^2/2$ (cf. Liang and Anderson 2007).

Second, the transfer term in our formalism conserves energy among scales, i.e., satisfying $\sum_\varpi \sum_n \Gamma_n^\varpi = 0$. This conservation property does not hold in traditional formalisms.

To illustrate, consider a scalar T in an incompressible fluid flow $\mathbf{u}$. Its evolution (ignore the diffusion) is governed by

$$\frac{\partial T}{\partial t} + \nabla\cdot(\mathbf{u}T) = 0. \tag{A2}$$

By performing Reynolds decomposition to separate T into a constant mean part $\underline{T}$ plus the departure from it T', the energy equations for the mean and eddy fields are

$$\frac{\partial}{\partial t}\left(\frac{1}{2}\underline{T}^2\right) + \nabla\cdot\left(\frac{1}{2}\underline{\mathbf{u}\,T^2}\right) = -\underline{T}\nabla\cdot(\underline{\mathbf{u}'\,T'}), \quad \text{and} \tag{A3}$$

$$\frac{\partial}{\partial t}\left(\frac{1}{2}\underline{T'^2}\right) + \nabla\cdot\left(\frac{1}{2}\underline{\mathbf{u}T'^2}\right) = -\underline{\mathbf{u}'\,T'}\cdot\nabla\underline{T}, \tag{A4}$$

respectively. The two terms on the right-hand side of Eqs. (A3) and (A4) denote the energy transfers associated with eddy–mean flow interactions. The two terms with divergence operator denote energy transport (or advection) in physical space. Obviously, the energy transfers in the mean and eddy equations do not cancel out, implying that the so-obtained transfer does not conserve energy among scales. This problem is not new and has long been realized in literature (e.g., Holopainen 1978; Plumb 1983). For instance, Plumb (1983) pointed out that the local expression of energy transfer is not unique, and hence may be physically irrelevant. Based on MWT, Liang (2016) proved, through reconstructing the "atomic" energy fluxes on the multiple scale windows, that a natural and unique separation exists. The resulting cross-scale transfer is

$$\Gamma_n^{\varpi} = \frac{1}{2}\left[\widehat{(\mathbf{u}T)}_n^{\sim\varpi}\cdot\nabla\widehat{T}_n^{\sim\varpi} - \widehat{T}_n^{\sim\varpi}\nabla\cdot\widehat{(\mathbf{u}T)}_n^{\sim\varpi}\right]. \tag{A5}$$

Based on (A5), Liang and Robinson (2007) showed that the energy equations for the Reynolds decomposition case (notice that Reynolds decomposition is a special form of the more generalized MWT):

$$\frac{\partial}{\partial t}\left(\frac{1}{2}\underline{T}^2\right) + \nabla\cdot\left(\frac{1}{2}\underline{\mathbf{u}\,T^2} + \frac{1}{2}\underline{T}\,\underline{\mathbf{u}'\,T'}\right) = -\Gamma, \quad \text{and} \tag{A6}$$

$$\frac{\partial}{\partial t}\left(\frac{1}{2}\underline{T'^2}\right) + \nabla\cdot\left(\frac{1}{2}\underline{\mathbf{u}T'^2} + \frac{1}{2}\underline{T}\,\underline{\mathbf{u}'T'}\right) = \Gamma, \tag{A7}$$

where $\Gamma = \{1/2[\underline{T}\nabla\cdot(\underline{\mathbf{u}'\,T'}) - \underline{\mathbf{u}'\,T'}\cdot\nabla\underline{T}]\}$ is the canonical transfer. Obviously, the right-hand side of Eqs. (A6) and (A7) is balanced and is hence a faithful representation of eddy–mean flow interaction processes. The canonical transfer has been validated with many benchmark processes. For example, Liang and Robinson (2007) demonstrated that, for a barotropic instability model whose instability structure is analytically known, the traditional transfer expression does not give the correct source of instability, while the canonical transfer does.

REFERENCES

Aguedjou, H. M. A., I. Dadou, A. Chaigneau, Y. Morel, and G. Alory, 2019: Eddies in the Tropical Atlantic Ocean and their seasonal variability. *Geophys. Res. Lett.*, **46**, 12 156–12 164, https://doi.org/10.1029/2019GL083925.

Aroucha, L. C., D. Veleda, F. S. Lopes, P. Tyaquiçã, N. Lefèvre, and M. Araujo, 2020: Intra- and inter-annual variability of North Brazil Current rings using angular momentum eddy detection and tracking algorithm: Observations from 1993 to 2016. *J. Geophys. Res. Oceans*, **125**, e2019JC015921, https://doi.org/10.1029/2019JC015921.

Barnier, B., T. Reynaud, A. Beckmann, C. Böning, J.-M. Molines, S. Barnard, and Y. Jia, 2001: On the seasonal variability and eddies in the North Brazil Current: Insights from model intercomparison experiments. *Prog. Oceanogr.*, **48**, 195–230, https://doi.org/10.1016/S0079-6611(01)00005-2.

Blockley, E. W., and Coauthors, 2014: Recent development of the Met Office operational ocean forecasting system: An overview and assessment of the new Global FOAM forecasts. *Geosci. Model Dev.*, **7**, 2613–2638, https://doi.org/10.5194/gmd-7-2613-2014.

Castelão, G. P., 2011: The internal structure, seasonality, and generation mechanisms of surface North Brazil Current rings. Ph.D. dissertation, University of Miami, 128 pp.

Chang, P., and Coauthors, 2008: Oceanic link between abrupt changes in the North Atlantic Ocean and the African monsoon. *Nat. Geosci.*, **1**, 444–448, https://doi.org/10.1038/ngeo218.

Chen, R., G. R. Flierl, and C. Wunsch, 2014: A description of local and nonlocal eddy–mean flow interaction in a global eddy-permitting state estimate. *J. Phys. Oceanogr.*, **44**, 2336–2352, https://doi.org/10.1175/JPO-D-14-0009.1.

Chen, X., B. Qiu, S. Chen, Y. Qi, and Y. Du, 2015: Seasonal eddy kinetic energy modulations along the North Equatorial Countercurrent in the western Pacific. *J. Geophys. Res. Oceans*, **120**, 6351–6362, https://doi.org/10.1002/2015JC011054.

Cummings, J. A., and O. M. Smedstad, 2013: Variational data assimilation for the global ocean. *Data Assimilation for Atmospheric, Oceanic and Hydrologic Applications*, Vol. II, S. Park and L. Xu, Eds., Springer, 303–343, https://doi.org/10.1007/978-3-642-35088-7_13.

da Silveira, I. C. A., W. S. Brown, and G. R. Flierl, 2000: Dynamics of the North Brazil Current retroflection region from the Western Tropical Atlantic Experiment observations. *J. Geophys. Res.*, **105**, 28 559–28 583, https://doi.org/10.1029/2000JC900129.

de Decco, H. T., A. R. Torres Jr., L. P. Pezzi, and L. Landau, 2018: Revisiting tropical instability wave variability in the Atlantic ocean using SODA reanalysis. *Ocean Dyn.*, **68**, 327–345, https://doi.org/10.1007/s10236-017-1128-2.

de Freitas Assad, L. P., R. Toste, C. S. Böck, D. M. Nehme, L. Sancho, A. E. Soares, and L. Landau, 2020: Ocean climatology at Brazilian equatorial margin: A numerical approach. *J. Comput. Sci.*, **44**, 101159, https://doi.org/10.1016/j.jocs.2020.101159.

Douglass, E. M., and J. G. Richman, 2015: Analysis of ageostrophy in strong surface eddies in the Atlantic Ocean. *J. Geophys. Res. Oceans*, **120**, 1490–1507, https://doi.org/10.1002/2014JC010350.

Febres-Ortega, G., and L. E. Herrera, 1976: Caribbean Sea circulation and water mass transports near the Lesser Antilles. *Bol. Inst. Oceanogr.*, **15**, 83–96.

Ferrari, R., and C. Wunsch, 2009: Ocean circulation kinetic energy: Reservoirs, sources, and sinks. *Annu. Rev. Fluid Mech.*,

41, 253–282, https://doi.org/10.1146/annurev.fluid.40.111406.102139.

Fratantoni, D. M., W. E. Johns, and T. L. Townsend, 1995: Rings of the North Brazil Current: Their structure and behavior inferred from observations and a numerical simulation. *J. Geophys. Res.*, **100**, 10 633–10 654, https://doi.org/10.1029/95JC00925.

Fu, Y., P. Brandt, F. P. Tuchen, J. F. Lübbecke, and C. Wang, 2022: Representation of the mean Atlantic subtropical cells in CMIP6 models. *J. Geophys. Res. Oceans*, **127**, e2021JC018191, https://doi.org/10.1029/2021JC018191.

Garzoli, S. L., A. Ffield, and Q. Yao, 2003: North Brazil Current rings and the variability in the latitude of retroflection. *Interhemispheric Water Exchange in the Atlantic Ocean*, G. J. Goni and P. Malanotte-Rizzoli, Eds., Elsevier Oceanography Series, Vol. 68, Elsevier, 357–373, https://doi.org/10.1016/S0422-9894(03)80154-X.

Goni, G. J., and W. E. Johns, 2001: A census of North Brazil Current rings observed from TOPEX/POSEIDON altimetry: 1992–1998. *Geophys. Res. Lett.*, **28**, 1–4, https://doi.org/10.1029/2000GL011717.

——, and ——, 2003: Synoptic study of warm rings in the North Brazil Current retroflection region using satellite altimetry. *Interhemispheric Water Exchange in the Atlantic Ocean*, G. J. Goni and P. Malanotte-Rizzoli, Eds., Elsevier Oceanography Series, Vol. 68, Elsevier, 335–356, https://doi.org/10.1016/S0422-9894(03)80153-8.

Holopainen, E. O., 1978: A diagnostic study of the kinetic energy balance of the long-term mean flow and the associated transient fluctuations in the atmosphere. *Geophysica*, **15**, 125–145.

Huang, M., X. Liang, Y. Zhu, Y. Liu, and R. H. Weisberg, 2021: Eddies connect the tropical Atlantic Ocean and the Gulf of Mexico. *Geophys. Res. Lett.*, **48**, e2020GL091277, https://doi.org/10.1029/2020GL091277.

Hüttl, S., and C. W. Böning, 2006: Mechanisms of decadal variability in the shallow subtropical-tropical circulation of the Atlantic Ocean: A model study. *J. Geophys. Res.*, **111**, C07011, https://doi.org/10.1029/2005JC003414.

Jochum, M., P. Malanotte-Rizzoli, and A. Busalacchi, 2004: Tropical instability waves in the Atlantic Ocean. *Ocean Modell.*, **7**, 145–163, https://doi.org/10.1016/S1463-5003(03)00042-8.

Jochumsen, K., M. Rhein, S. Hüttl-Kabus, and C. W. Böning, 2010: On the propagation and decay of North Brazil Current rings. *J. Geophys. Res.*, **115**, C10004, https://doi.org/10.1029/2009JC006042.

Johns, W. E., T. N. Lee, F. A. Schott, R. J. Zantopp, and R. H. Evans, 1990: The North Brazil Current retroflection: Seasonal structure and eddy variability. *J. Geophys. Res.*, **95**, 22 103–22 120, https://doi.org/10.1029/JC095iC12p22103.

——, ——, R. C. Beardsley, J. Candela, R. Limeburner, and B. Castro, 1998: Annual cycle and variability of the North Brazil Current. *J. Phys. Oceanogr.*, **28**, 103–128, https://doi.org/10.1175/1520-0485(1998)028<0103:ACAVOT>2.0.CO;2.

——, T. L. Townsend, D. M. Fratantoni, and W. D. Wilson, 2002: On the Atlantic inflow to the Caribbean Sea. *Deep-Sea Res. I*, **49**, 211–243, https://doi.org/10.1016/S0967-0637(01)00041-3.

Jouanno, J., J. Sheinbaum, B. Barnier, J. M. Molines, and J. Candela, 2012: Seasonal and Interannual modulation of the eddy kinetic energy in the Caribbean Sea. *J. Phys. Oceanogr.*, **42**, 2041–2055, https://doi.org/10.1175/JPO-D-12-048.1.

Kang, D., and E. N. Curchitser, 2017: On the evaluation of seasonal variability of the ocean kinetic energy. *J. Phys. Oceanogr.*, **47**, 1675–1683, https://doi.org/10.1175/JPO-D-17-0063.1.

——, ——, and A. Rosati, 2016: Seasonal variability of the Gulf Stream kinetic energy. *J. Phys. Oceanogr.*, **46**, 1189–1207, https://doi.org/10.1175/JPO-D-15-0235.1.

Körner, M., M. Claus, P. Brandt, and F. P. Tuchen, 2022: Sources and pathways of intraseasonal meridional kinetic energy in the equatorial Atlantic Ocean. *J. Phys. Oceanogr.*, **52**, 2445–2462, https://doi.org/10.1175/JPO-D-21-0315.1.

Lellouche, J.-M., and Coauthors, 2013: Evaluation of global monitoring and forecasting systems at Mercator Océan. *Ocean Sci.*, **9**, 57–81, https://doi.org/10.5194/os-9-57-2013.

Liang, X., 2016: Canonical transfer and multiscale energetics for primitive and quasigeostrophic atmospheres. *J. Atmos. Sci.*, **73**, 4439–4468, https://doi.org/10.1175/JAS-D-16-0131.1.

——, and A. R. Robinson, 2007: Localized multi-scale energy and vorticity analysis: II. Finite-amplitude instability theory and validation. *Dyn. Atmos. Oceans*, **44**, 51–76, https://doi.org/10.1016/j.dynatmoce.2007.04.001.

——, and D. G. M. Anderson, 2007: Multiscale window transform. *Multiscale Model. Simul.*, **6**, 437–467, https://doi.org/10.1137/06066895X.

——, and A. R. Robinson, 2009: Multiscale processes and nonlinear dynamics of the circulation and upwelling events off Monterey Bay. *J. Phys. Oceanogr.*, **39**, 290–313, https://doi.org/10.1175/2008JPO3950.1.

Liu, Y., X. Liang, and R. H. Weisberg, 2007: Rectification of the bias in the wavelet power spectrum. *J. Atmos. Oceanic Technol.*, **24**, 2093–2102, https://doi.org/10.1175/2007JTECHO511.1.

Lorenz, E. N., 1955: Available potential energy and the maintenance of the general circulation. *Tellus*, **7**, 157–167, https://doi.org/10.3402/tellusa.v7i2.8796.

Ma, J., and X. Liang, 2017: Multiscale dynamical processes underlying the wintertime Atlantic blockings. *J. Atmos. Sci.*, **74**, 3815–3831, https://doi.org/10.1175/JAS-D-16-0295.1.

Marshall, J., A. Adcroft, C. Hill, L. Perelman, and C. Heisey, 1997: A finite-volume, incompressible Navier Stokes model for studies of the ocean on parallel computers. *J. Geophys. Res.*, **102**, 5753–5766, https://doi.org/10.1029/96JC02775.

McWilliams, J. C., 2016: Submesoscale currents in the ocean. *Proc. Roy. Soc.*, **472A**, 20160117, https://doi.org/10.1098/rspa.2016.0117.

Mélice, J.-L., and S. Arnault, 2017: Investigation of the intra-annual variability of the North Equatorial countercurrent/North Brazil Current eddies and of the instability waves of the North Tropical Atlantic Ocean using satellite altimetry and empirical mode decomposition. *J. Atmos. Oceanic Technol.*, **34**, 2295–2310, https://doi.org/10.1175/JTECH-D-17-0032.1.

Menemenlis, D., J. Campin, P. Heimbach, C. Hill, T. Lee, A. Nguyen, M. Schodlock, and H. Zhang, 2008: ECCO2: High resolution global ocean and sea ice data synthesis. *Mercator Ocean Quarterly Newsletter*, No. 31, Mercator Ocean, Ramonville Saint-Agne, France, 13–21.

Metzger, E. J., and Coauthors., 2014: US Navy operational global ocean and Arctic ice prediction systems. *Oceanography*, **27**, 32–43, https://doi.org/10.5670/oceanog.2014.66.

Murphy, S. J., H. E. Hurlburt, and J. J. O'Brien, 1999: The connectivity of eddy variability in the Caribbean Sea, the Gulf of Mexico, and the Atlantic Ocean. *J. Geophys. Res.*, **104**, 1431–1453, https://doi.org/10.1029/1998JC900010.

Nencioli, F., C. Dong, T. Dickey, L. Washburn, and J. C. McWilliams, 2010: A vector geometry–based eddy detection algorithm and its application to a high-resolution numerical model product and high-frequency radar surface velocities in the Southern

California Bight. *J. Atmos. Oceanic Technol.*, **27**, 564–579, https://doi.org/10.1175/2009JTECHO725.1.

Plumb, R. A., 1983: A new look at the energy cycle. *J. Atmos. Sci.*, **40**, 1669–1688, https://doi.org/10.1175/1520-0469(1983)040<1669:ANLATE>2.0.CO;2.

Pujol, M.-I., Y. Faugère, G. Taburet, S. Dupuy, C. Pelloquin, M. Ablain, and N. Picot, 2016: DUACS DT2014: The new multi-mission altimeter data set reprocessed over 20 years. *Ocean Sci.*, **12**, 1067–1090, https://doi.org/10.5194/os-12-1067-2016.

Qiu, B., S. Chen, P. Klein, H. Sasaki, and Y. Sasai, 2014: Seasonal mesoscale and submesoscale eddy variability along the North Pacific subtropical countercurrent. *J. Phys. Oceanogr.*, **44**, 3079–3098, https://doi.org/10.1175/JPO-D-14-0071.1.

Richardson, P. L., and D. Walsh, 1986: Mapping climatological seasonal variations of surface currents in the tropical Atlantic using ship drifts. *J. Geophys. Res.*, **91**, 10 537–10 550, https://doi.org/10.1029/JC091iC09p10537.

——, G. E. Hufford, R. Limeburner, and W. S. Brown, 1994: North Brazil Current retroflection eddies. *J. Geophys. Res.*, **99**, 5081–5093, https://doi.org/10.1029/93JC03486.

Rieck, J. K., C. W. Böning, R. J. Greatbatch, and M. Scheinert, 2015: Seasonal variability of eddy kinetic energy in a global high-resolution ocean model. *Geophys. Res. Lett.*, **42**, 9379–9386, https://doi.org/10.1002/2015GL066152.

Rosell-Fieschi, M., J. L. Pelegrí, and J. Gourrion, 2015: Zonal jets in the equatorial Atlantic Ocean. *Prog. Oceanogr.*, **130**, 1–18, https://doi.org/10.1016/j.pocean.2014.08.008.

Rühs, S., J. V. Durgadoo, E. Behrens, and A. Biastoch, 2013: Advective timescales and pathways of Agulhas leakage *Geophys. Res. Lett.*, **40**, 3997–4000, https://doi.org/10.1002/grl.50782.

——, K. Getzlaff, J. V. Durgadoo, A. Biastoch, and C. W. Böning, 2015: On the suitability of North Brazil Current transport estimates for monitoring basin-scale AMOC changes. *Geophys. Res. Lett.*, **42**, 8072–8080, https://doi.org/10.1002/2015GL065695.

Sasaki, H., P. Klein, B. Qiu, and Y. Sasai, 2014: Impact of oceanic-scale interactions on the seasonal modulation of ocean dynamics by the atmosphere. *Nat. Commun.*, **5**, 5636, https://doi.org/10.1038/ncomms6636.

——, ——, Y. Sasai, and B. Qiu, 2017: Regionality and seasonality of submesoscale and mesoscale turbulence in the North Pacific Ocean. *Ocean Dyn.*, **67**, 1195–1216, https://doi.org/10.1007/s10236-017-1083-y.

Sharma, N., S. P. Anderson, P. Brickley, C. Nobre, and M. L. Cadwallader, 2009: Quantifying the seasonal and interannual variability of the formation and migration pattern of North Brazil Current rings. *OCEANS 2009*, Biloxi, MS, Institute of Electrical and Electronics Engineers, 1–7, https://doi.org/10.23919/OCEANS.2009.5422142.

Storto, A., and S. Masina, 2016: C-GLORSv5: An improved multipurpose global ocean eddy-permitting physical reanalysis. *Earth Syst. Sci. Data*, **8**, 679–696, https://doi.org/10.5194/essd-8-679-2016.

Tuchen, F. P., J. F. Lübbecke, P. Brandt, and Y. Fu, 2020: Observed transport variability of the Atlantic subtropical cells and their connection to tropical sea surface temperature variability. *J. Geophys. Res. Oceans*, **125**, e2020JC016592, https://doi.org/10.1029/2020JC016592.

——, P. Brandt, J. F. Lübbecke, and R. Hummels, 2022: Transports and pathways of the tropical AMOC return flow from Argo data and shipboard velocity measurements. *J. Geophys. Res. Oceans*, **127**, e2021JC018115, https://doi.org/10.1029/2021JC018115.

Vallès-Casanova, I., E. Fraile-Nuez, M. Martín-Rey, E. van Sebille, A. Cabré, A. Olivé-Abelló, and J. L. Pelegrí, 2022: Water mass transports and pathways in the North Brazil-Equatorial Undercurrent retroflection. *J. Geophys. Res. Oceans*, **127**, e2021JC018150, https://doi.org/10.1029/2021JC018150.

van der Boog, C. G., and Coauthors, 2019: The impact of upwelling on the intensification of anticyclonic ocean eddies in the Caribbean Sea. *Ocean Sci.*, **15**, 1419–1437, https://doi.org/10.5194/os-15-1419-2019.

——, M. J. Molemaker, H. A. Dijkstra, J. D. Pietrzak, and C. A. Katsman, 2022: Generation of vorticity near topography: Anticyclones in the Caribbean Sea. *J. Geophys. Res. Oceans*, **127**, e2021JC017987, https://doi.org/10.1029/2021JC017987.

van Westen, R. M., and Coauthors, 2018: Mechanisms of the 40–70 day variability in the Yucatan Channel volume transport. *J. Geophys. Res. Oceans*, **123**, 1286–1300, https://doi.org/10.1002/2017JC013580.

von Schuckmann, K., P. Brandt, and C. Eden, 2008: Generation of tropical instability waves in the Atlantic Ocean. *J. Geophys. Res.*, **113**, C08034, https://doi.org/10.1029/2007JC004712.

von Storch, J.-S., C. Eden, I. Fast, H. Haak, D. Hernández-Deckers, E. Maier-Reimer, J. Marotzke, and D. Stammer, 2012: An estimate of the Lorenz energy cycle for the world ocean based on the STORM/NCEP simulation. *J. Phys. Oceanogr.*, **42**, 2185–2205, https://doi.org/10.1175/JPO-D-12-079.1.

Wang, Q., and S. Pierini, 2020: On the role of the Kuroshio extension bimodality in modulating the surface eddy kinetic energy seasonal variability. *Geophys. Res. Lett.*, **47**, e2019GL086308, https://doi.org/10.1029/2019GL086308.

Wang, S., Z. Jing, Q. Zhang, P. Chang, Z. Chen, H. Liu, and L. Wu, 2019: Ocean eddy energetics in the spectral space as revealed by high-resolution general circulation models. *J. Phys. Oceanogr.*, **49**, 2815–2827, https://doi.org/10.1175/JPO-D-19-0034.1.

Wilson, W. D., and W. E. Johns, 1997: Velocity structure and transport in the Windward Islands passages. *Deep-Sea Res.*, **44A**, 487–520, https://doi.org/10.1016/S0967-0637(96)00113-6.

——, ——, and S. L. Garzoli, 2002: Velocity structure of North Brazil Current rings. *Geophys. Res. Lett.*, **29**, 114–1–114–4, https://doi.org/10.1029/2001GL013869.

Wunsch, C., P. Heimbach, R. M. Ponte, and I. Fukumori, 2009: The global general circulation of the ocean estimated by the ECCO-consortium. *Oceanography*, **22**, 88–103, https://doi.org/10.5670/oceanog.2009.41.

Xu, F., and X. Liang, 2017: On the generation and maintenance of the 2012/13 sudden stratospheric warming. *J. Atmos. Sci.*, **74**, 3209–3228, https://doi.org/10.1175/JAS-D-17-0002.1.

Yang, Y., and X. Liang, 2018: On the seasonal eddy variability in the Kuroshio extension. *J. Phys. Oceanogr.*, **48**, 1675–1689, https://doi.org/10.1175/JPO-D-18-0058.1.

——, and ——, 2019a: New perspectives on the generation and maintenance of the Kuroshio large meander. *J. Phys. Oceanogr.*, **49**, 2095–2113, https://doi.org/10.1175/JPO-D-18-0276.1.

——, and ——, 2019b: Spatiotemporal variability of the global ocean internal processes inferred from satellite observations. *J. Phys. Oceanogr.*, **49**, 2147–2164, https://doi.org/10.1175/JPO-D-18-0273.1.

——, ——, B. Qiu, and S. Chen, 2017: On the decadal variability of the eddy kinetic energy in the Kuroshio Extension. *J. Phys. Oceanogr.*, **47**, 1169–1187, https://doi.org/10.1175/JPO-D-16-0201.1.

——, R. H. Weisberg, Y. Liu, and X. Liang, 2020: Instabilities and multiscale interactions underlying the loop current eddy shedding in the Gulf of Mexico. *J. Phys. Oceanogr.*, **50**, 1289–1317, https://doi.org/10.1175/JPO-D-19-0202.1.

Zhang, D., R. Msadek, M. J. McPhaden, and T. Delworth, 2011: Multidecadal variability of the North Brazil Current and its connection to the Atlantic meridional overturning circulation. *J. Geophys. Res.*, **116**, C04012, https://doi.org/10.1029/2010JC006812.

Zhang, L., Y. Hui, T. Qu, and D. Hu, 2021: Seasonal variability of subthermocline eddy kinetic energy east of the Philippines. *J. Phys. Oceanogr.*, **51**, 685–699, https://doi.org/10.1175/JPO-D-20-0101.1.

Zhao, Y.-B., X. Liang, and J. Gan, 2016: Nonlinear multiscale interactions and internal dynamics underlying a typical eddy-shedding event at Luzon Strait. *J. Geophys. Res. Oceans*, **121**, 8208–8229, https://doi.org/10.1002/2016JC012483.

Zhao, Y., Y. Yang, X. Liang, and Y. Zhang, 2022: Different mechanisms for the seasonal variations of the mesoscale eddy energy in the South China Sea. *Deep-Sea Res. I*, **179**, 103677, https://doi.org/10.1016/j.dsr.2021.103677.

Zuo, H., M. A. Balmaseda, S. Tietsche, K. Mogensen, and M. Mayer, 2019: The ECMWF operational ensemble reanalysis-analysis system for ocean and sea-ice: A description of the system and assessment. *Ocean Sci.*, **15**, 779–808, https://doi.org/10.5194/os-15-779-2019.